Propellants, Explosives, Pyrotechnics

WILEY-VCH

Propellants, Explosives, Pyrotechnics

RESEARCH ARTICLE OPEN ACCESS

AWSD Reactive Burn Model for High Explosive LX-14

Galen T Craven | Christopher Ticknor

Theoretical Division, Los Alamos National Laboratory, Los Alamos, New Mexico, USA

Correspondence: Galen T Craven (gcraven@lanl.gov) | Christopher Ticknor (cticknor@lanl.gov)

Received: 25 September 2024 | **Accepted:** 22 November 2024

Funding: This work was supported by the U.S. Department of Energy through the Los Alamos National Laboratory.

Keywords: high explosive | HMX | LX-14

ABSTRACT

The results of an Arrhenius–Wescott–Stewart–Davis (AWSD) reactive flow calibration for the HMX-based high explosive LX-14 are presented. The parameters in the AWSD model are calibrated to experimental thermodynamic and gas gun data and to computational results from thermochemical calculations. There is no experimental rate stick data available for LX-14; therefore, scaled experimental results from other PBX-based high explosives are used in the calibration to fill this gap in data. Strong agreement is observed between the calibrated AWSD model and experimental data for LX-14, including validation data that were not used in the calibration procedure. The developed model more accurately describes experimental shock-to-detonation results compared to several other reactive flow models for LX-14 from the literature. The presented results illustrate that the AWSD model is capable of quantitatively describing the reactive burn of LX-14.

1 | Introduction

LX-14 is an HMX-based high explosive (HE) consisting of 95.5% HMX and 4.5% estane binder by weight. It was designed to have high energy, low shock sensitivity and improved mechanical properties compared to other HEs such as PBX 9404 [1, 2]. LX-14 is similar in chemical structure to PBX 9501 but has a less reactive binder [3]. The typical density of LX-14 is approximately 1.830 g cm^{-3} in pressed charges [4]. Several recent studies have been performed to assess the performance of LX-14 [3–8]. Because of its potential importance, a number of theoretical tools and reactive models have been applied to predict the performance of LX-14 with varying degrees of success [4, 6–8].

Reactive flow models are used to understand and predict the performance of energetic materials and HEs. Here, we develop a reactive flow model for LX-14 using the Arrhenius–Wescott–Stewart–Davis (AWSD) model [9, 10]. In the AWSD model, kinetic properties in the reaction rate equations are coupled with thermodynamic equations of state to predict the behavior of a material, typically an HE, under various thermodynamic and shock conditions. The AWSD model uses a Davis reactants equation of state (EOS), and a Davis products EOS coupled with an Arrhenius rate law [11–13] to describe the burn of the target material [14–16]. The parameters in the AWSD model must be calibrated to the specific material under investigation. Calibrated AWSD models have recently been applied with success to model shock-to-detonation (SDT) behavior and other thermodynamic and mechanical properties in several HEs [10, 17], with the results of those calibrations being in strong agreement with experimental data. The AWSD model has limitations including being unable to accurately describe the relations between thermodynamic quantities and their derivatives in some systems and also being unable to capture nonequilibrium chemical kinetics due to equilibrium assumptions in the Arrhenius rate law [18–22]. The AWSD model is a particular theoretical tool in the broad field of computational treatments of shock-induced chemical reactions and HE detonations [9, 12, 23–28].

There are four reactive flow models for LX-14 in the open literature: (1) a CREST model [8], (2) a Scaled Uniform Reactive Flow (SURF) model [4], (3) an Ignition & Growth (I&G) model by Vandersall et al. [6], and (4) an I&G model by Tarver [7]. Handley and Whitworth used the CREST entropy-dependent reactive burn model to examine the reactive flow of LX-14 [8]. The CREST model accurately predicted the behavior of LX-14 at nominal density. The shapes of the shock to detonation curves were in good agreement with experimental data, but the run-to-detonation distances were not accurately predicted. Jones et al. compared a SURF model [4] calibration of LX-14 to embedded particle velocity gauge data. The LX-14 SURF model used PBX 9501 parameters with one modification. The model reproduced the measured LX-14 wave profiles from a qualitative standpoint, a manifestation of the close chemical relationship between LX-14 and PBX 9501. The SURF model reproduced some detonation observables well, but the amplitude of the particle velocity in the gas gun wavefronts was not accurate. Vandersall et al. and Tarver both developed different I&G models for LX-14. Vandersall performed embedded manganin pressure gauge experiments and calibrated an I&G model. Tarver showed that embedded manganin pressure gauge and embedded particle velocity gauge measurements yielded equivalent results for LX-14 and calibrated an I&G model that gave generally good predictions for the shapes of the shock-to-detonation curves [7].

Here, we present results of an AWSD reactive flow calibration for LX-14. The model is calibrated to experimental data from various sources and to thermochemical data generated using the MAGPIE code [29]. Kinetic parameters in the model, that is, in the Arrhenius rate law describing the reactive burn, are calibrated to the series of gas gun shots performed by Jones et al. at Los Alamos National Laboratory [4]. We are not aware of any available rate stick data for LX-14, so we use scaled values from other PBX-based explosives in the calibration to fill this gap in data. Strong agreement is observed between the calibrated model and experimental data from multiple sources, suggesting that the AWSD model is capable of accurately describing the reactive burn of LX-14. The results from the AWSD model are qualitatively compared with other reactive flow models for LX-14. We also compare the LX-14 and PBX 9501 AWSD models throughout, illustrating both similarities and differences in the behavior of these two HEs. We find that our calibrated LX-14 AWSD model often outperforms other LX-14 reactive flow models, offering predictive improvements with respect to several detonation properties.

The remainder of this article is organized as follows: Section 2.1 contains the details of the reactants EOS calibration. Section 2.2 contains the details of the products EOS calibration. In Section 2.3, the results of the AWSD rate law calibration are presented, focusing on shock-to-detonation and diameter effect results. Conclusions are discussed in Section 3.

2 | AWSD Model Calibration

We follow the mathematical exposition of the AWSD model given in [10] and [30]. For completeness, all of the equations used in the model along with brief descriptions are reproduced here. The general calibration procedure we use for the parameters in the model follows [31]. The calibrated parameter values are specific to LX-14.

2.1 | Reactants EOS

The Davis reactants EOS model is a Mie–Grüneisen EOS with energy given by

$$e_{\mathrm{R}}(p,\rho) = e_{\mathrm{R}}^{(s)}(\rho) + \frac{p - p_{\mathrm{R}}^{(s)}}{\rho\Gamma_{\mathrm{R}}(\rho)}, \tag{1}$$

and pressure is given by

$$p_{\mathrm{R}}(e,\rho) = p_{\mathrm{R}}^{(s)}(\rho) + \rho\Gamma_{\mathrm{R}}(\rho)\Big(e - e_{\mathrm{R}}^{(s)}(\rho)\Big), \tag{2}$$

where $\Gamma_{\mathrm{R}}(\rho)$ is the Grüneisen gamma function and subscript "R" denotes the reactant state. The energy on the reference isentrope is

$$e_{\mathrm{R}}^{(s)}(\rho) = E_{\mathrm{det}} + \int_{\rho_0}^{\rho} \frac{p_{\mathrm{R}}^{(s)}}{\bar{\rho}^2}\, d\bar{\rho}, \tag{3}$$

where E_{det} is the stored chemical potential energy of the material and the superscript "s" denotes that the quantity is calculated along the isentrope. The pressure on the isentrope is given by the piecewise function

$$p_{\mathrm{R}}^{(s)}(\rho) = \begin{cases} \hat{p}[\exp(4By) - 1], & \rho < \rho_0, \\ \hat{p}\left[\sum_{j=1}^{3} \frac{(4By)^j}{j!} + C\frac{(4By)^4}{4!} + \frac{y^2}{(1-y)^4}\right], & \rho \geq \rho_0, \end{cases} \tag{4}$$

where $y = 1 - \rho_0/\rho$ and $\hat{p} = \rho_0 A^2/4B$. The Grüneisen gamma function is given by the piecewise form

$$\Gamma_{\mathrm{R}}^{(s)}(\rho) = \begin{cases} \Gamma_0, & \rho < \rho_0, \\ \Gamma_0 + Zy, & \rho \geq \rho_0. \end{cases} \tag{5}$$

The temperature of the reactants is

$$T_{\mathrm{R}}(e,\rho) = T_{\mathrm{R}}^{(s)}(\rho)\left(\frac{1+\alpha_{st}}{C_v^{(0)} T_{\mathrm{R}}^{(s)}(\rho)}\Big(e - e_{\mathrm{R}}^{(s)}(\rho)\Big) + 1\right)^{\frac{1}{1+\alpha_{st}}}, \tag{6}$$

where

$$T_{\mathrm{R}}^{(s)}(\rho) = T_0 \exp(-Zy)\left(\frac{\rho}{\rho_0}\right)^{(\Gamma_0 + Z)}, \tag{7}$$

is the temperature along the isentrope. Therefore, the Davis reactants EOS has 10 parameters: A, B, C, $C_v^{(0)}$, Γ_0, Z, α_{st}, ρ_0, T_0, and E_{det}. Values for these parameters can be obtained by calibrating the EOS model to experimental data, thermochemical calculations, simulation data, or a combination of these sources.

The parameter A is the ambient sound speed. It can be taken as the intercept of the U_{S}-U_{P} Hugoniot curve. Performing a linear fit to the data from [4] results in a value of $A = 2.85$ km s^{-1} for LX-14. Noting that this value was not in agreement with literature values, we instead used a value of $A = 2.494$ km s^{-1} taken from [4]. The

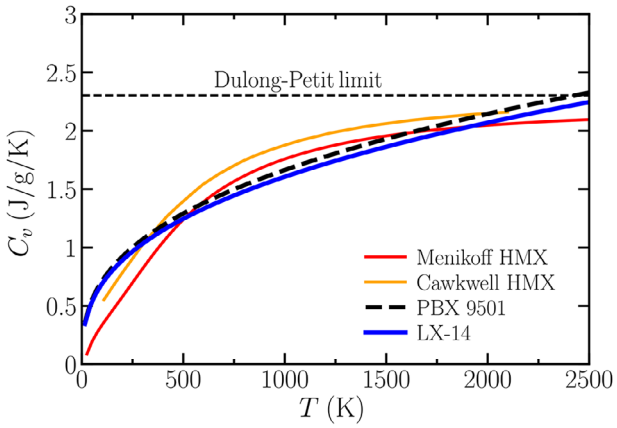

FIGURE 1 | The AWSD specific heat model for LX-14 is shown in blue. For comparison, results are also shown for the Menikoff HMX model (red) [32], the Cawkwell HMX model (orange) [33], and the AWSD result for PBX 9501 (dashed black) [31].

parameter B is the slope of the Hugoniot curve in the U_S-U_P plane at small U_P. A linear fit to the available LX-14 data generated a value of $B = 2.059$. The value of $\Gamma_0 = 0.862$ was taken directly from [4]. The nominal density of LX-14 is $\rho_0 = 1.830\ \mathrm{g\,cm^{-3}}$.

The specific heat in the Davis EOS model is given by

$$C_v(T) = C_v^{(0)}\left(\frac{T}{T_0}\right)^{\alpha_{st}}, \tag{8}$$

which is a function of temperature T and has three tunable parameters: T_0, $C_v^{(0)}$, and α_{st}. The nominal temperature T_0 was taken to be the ambient temperature. The heat at the reference volume $C_v^{(0)}$ and the value of α_{st} are constants that are determined based on the specific compound/material being modeled. There are no available experimental values for the constant volume specific heat of LX-14, so we instead calibrated to specific heat values for HMX. Specifically, we fit the parameters $C_v^{(0)}$ and α_{st} to data generated using the HMX specific heat model developed by Menikoff [32]. The optimization was performed using Nelder–Mead optimization starting from the PBX 9501 specific heat parameter values as the initial guess [31]. This procedure resulted in values of $C_v^{(0)} = 0.001031$ kJ/g/K and $\alpha_{st} = 0.3662$.

The calibrated Davis EOS specific heat model for LX-14 and the Menikoff HMX model are shown in Figure 1. For comparison, the HMX model developed by Cawkwellet al.[33] and the Davis EOS specific heat model for PBX 9501 calibrated in [31] are also shown. The Dulong–Petit limit for HMX is shown as a horizontal dashed black line. The Cawkwell and Menikoff HMX specific heat models both approach the Dulong–Petit limit as $T \to \infty$. However, the Davis EOS models for both LX-14 and PBX9501 exceed the Dulong–Petit limit at high temperatures, a known limitation of the functional form for the Davis EOS specific heat given in Equation (8).

The value of the parameter C was obtained by holding all other previously calibrated parameters constant and applying the Broyden–Fletcher–Goldfarb–Shanno optimization algorithm with the target goal of matching the EOS data from Jones et al.

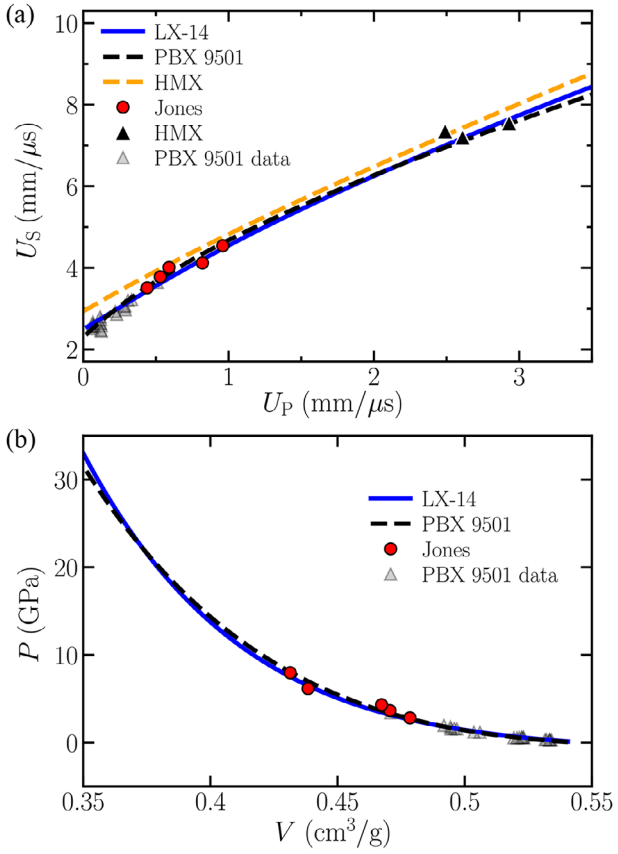

FIGURE 2 | Hugoniot curves for LX-14 reactants EOS calibrations in the (a) U_S-U_P and (b) P-V planes. The blue curves are the Davis EOS calibration for LX-14 performed in this work. The dashed black curves are the Davis EOS calibration for PBX 9501 performed in [31]. The red circular markers correspond to experimental data for LX-14 [4]. The black triangular markers in (a) correspond to HMX single crystal data from [34]. The gray triangular markers correspond to PBX 9501 experimental data from [35].

[4]. The initial guess for C was taken to be the value for PBX 9501 from [31]. This procedure resulted in a value $C = 4.591$ for LX-14.

Results from the calibrated LX-14 reactants EOS are shown in Figure 2. Figure 2a shows the Hugoniot curve in the U_S-U_P plane, where U_S is the shock velocity and U_P is the particle velocity. The red circular markers correspond to experimental data for LX-14, and the black triangular markers correspond to HMX single crystal data [4, 34]. The gray triangular markers are experimental data for PBX 9501 [35]. Comparing the PBX-9501 curve (dashed black) with the LX-14 curve (solid blue), the behavior of LX-14 is similar to PBX 9501. At small U_P values, the PBX 9501 Hugoniot varies nonlinearly while LX-14 is more linear. Outside of this nonlinear regime, the PBX 9501 and LX-14 Hugoniot curves are similar in magnitude and functional behavior. The orange dashed line is the result for HMX calculated using the `MAGPIE` code and is shown for comparison [29]. Figure 2b illustrates the Hugoniot curves in the P-V plane, where P is pressure and V is specific volume. As the specific volume becomes smaller, the LX-14 pressure exceeds the PBX 9501 pressure.

Shown in Figure 3 is a comparison between the U_S-U_P curves for LX-14 and PBX 9501 at small U_P. This plot highlights that the

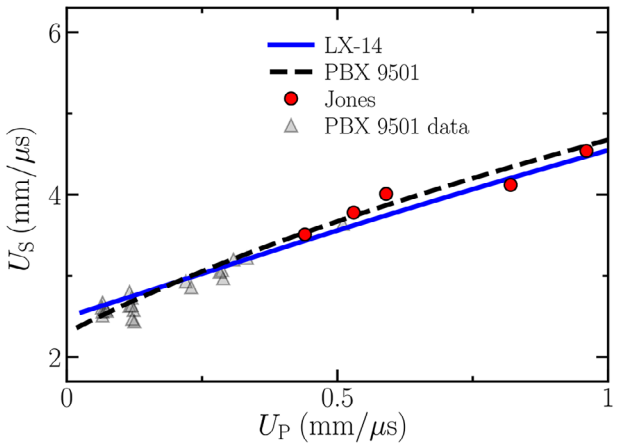

FIGURE 3 | U_S-U_P curve for the LX-14 reactants EOS at small U_P. The blue curve is the Davis EOS calibration for LX-14 performed in this work. The dashed black curve is the Davis EOS calibration for PBX 9501 performed in [31]. The red circular markers correspond to experimental data for LX-14 [4]. The gray triangular markers correspond to PBX 9501 experimental data from [35].

TABLE 1 | Reactants EOS parameters.

Parameter	Value	Unit
A	2.494	km s^{-1}
B	2.059	
C	4.591	
$C_v^{(0)}$	0.001031	kJ g^{-1} K^{-1}
Γ_0	0.8620	
Z	0	
α_{st}	0.3662	
ρ_0	1.830	g cm^{-3}
T_0	298.15	K
E_{det}	6.247	kJ g^{-1}

performance of LX-14 is more linear than PBX 9501 at small U_P (< 1 km s^{-1}) when comparing the Davis EOS models calibrated for each HE. For comparison, the sound speed value, that is, the U_S-U_P intercept, is 2.3 km s^{-1} for PBX 9501. The AWSD parameter B, which is the slope of the U_S-U_P Hugoniot curve as $U_P \to 0$, is 2.059 for LX-14 and 3.3 for PBX 9501.

A complete list of the parameters and parameter values used in the LX-14 Davis reactants EOS is given in Table 1.

2.2 | Products EOS

The Davis products EOS model is a Mie–Grüneisen EOS with energy given by

$$e_P(p,\rho) = e_P^{(s)}(\rho) + \frac{p - p_P^{(s)}}{\rho\Gamma_P(\rho)}, \tag{9}$$

and pressure is given by

$$p_P(e,\rho) = p_P^{(s)}(\rho) + \rho\Gamma_P(\rho)\left(e - e_P^{(s)}(\rho)\right), \tag{10}$$

where the subscript "P" denotes the products state and $\Gamma_P(\rho)$ is the Grüneisen gamma. The pressure on principal Chapman–Jouguet (CJ) isentrope is

$$p_P^{(s)}(\rho) = p_c \frac{\left[\frac{(\rho v_c)^{-n}}{2} + \frac{(\rho v_c)^n}{2}\right]^{a/n}}{(\rho v_c)^{-(k+a)}} \left(\frac{k-1+F(\rho)}{k-1+a}\right), \tag{11}$$

where

$$F(\rho) = \frac{2a(\rho v_c)^n}{(\rho v_c)^{-n} + (\rho v_c)^n}. \tag{12}$$

The Grüneisen gamma depends only on the density,

$$\Gamma_P(\rho) = k - 1 + (1-b)F(\rho). \tag{13}$$

The energy on the isentrope is

$$e_P^{(s)}(\rho) = e_c \frac{\left[\frac{(\rho v_c)^{-n}}{2} + \frac{(\rho v_c)^n}{2}\right]^{a/n}}{(\rho v_c)^{-(k-1+a)}}, \tag{14}$$

with

$$e_c = \frac{p_c v_c}{k-1+a}. \tag{15}$$

The temperature of the products is

$$T_P(e,\rho) = T_P^{(s)}(\rho) + \frac{e - e_P^{(s)}(\rho)}{C_{vp}}, \tag{16}$$

and the temperature on the principal isentrope is

$$T_P^{(s)}(\rho) = T_c \frac{\left[\frac{(\rho v_c)^{-n}}{2} + \frac{(\rho v_c)^n}{2}\right]^{(a/n)(1-b)}}{(\rho v_c)^{-(k-1+a(1-b))}}, \tag{17}$$

with

$$T_c = \left(\frac{2^{-ab/n}}{k-1+a}\right)\left(\frac{p_c v_c}{C_{vp}}\right). \tag{18}$$

The Davis products EOS has seven parameters: a, b, k, n, p_c, v_c, and C_{vp}, that must be calibrated by fitting the EOS model to available data sources. Here, we used the limited experimental data for LX-14 from Green et al. [36] coupled with thermochemical data generated using the code `MAGPIE`. The Davis products EOS was calibrated to that combined dataset. A Nelder–Mead algorithm was used to perform the EOS parameter optimization.

Results from the calibrated LX-14 products EOS are shown in Figure 4. Figure 4a shows the products Hugoniot curve in the U_S-U_P plane. The two red circular markers correspond to experimental data for LX-14 and the gray triangular markers are experimental data for PBX 9501, shown for comparison [36–38]. Comparing the calibrated LX-14 EOS curve (solid blue) with the

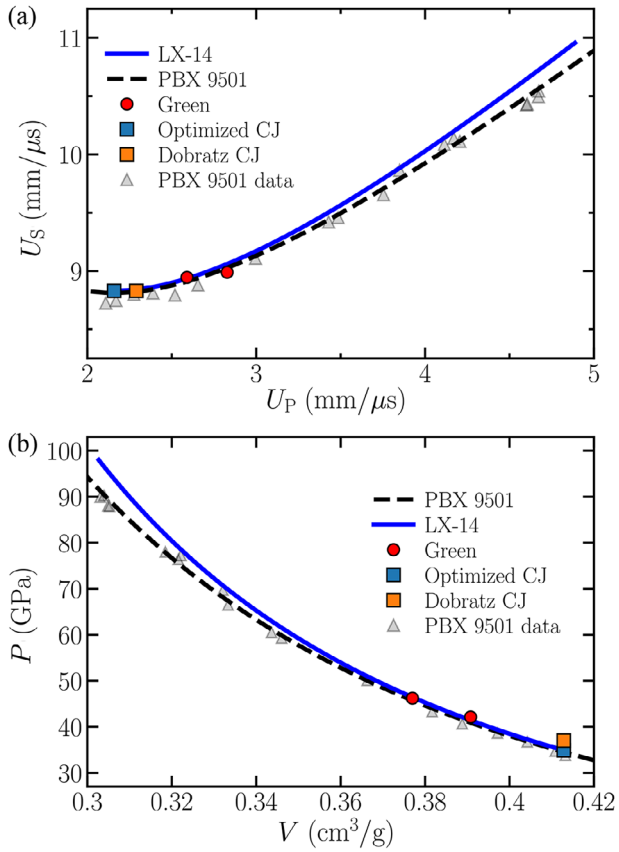

FIGURE 4 | Hugoniot curves for LX-14 products EOS calibrations in the (a) U_S-U_P and (b) P-V planes. The blue curves are the Davis EOS calibration for LX-14 performed in this work. The dashed black curves are the Davis EOS calibration for PBX 9501 [31]. The red circular markers correspond to experimental data for LX-14 [36]. The gray triangular markers correspond to PBX 9501 experimental data [37, 38]. The orange square marker is the CJ state reported by Dobratz [39], and the blue square marker is the CJ state calculated in this work.

PBX 9501 EOS curve (dashed black), it can be seen that the shock velocity of the LX-14 products is greater than PBX 9501 for the same particle velocity. The LX-14 CJ state given by Dobratz is shown as a square orange marker and the corresponding state is calculated using the calibrated/optimized Davis EOS is shown as a square blue marker. The detonation velocity from Dobratz is $D_{\mathrm{CJ}}^{\mathrm{Dobratz}} = 8.83\ \mathrm{km\,s^{-1}}$ and the optimized value is $D_{\mathrm{CJ}} = 8.829\ \mathrm{km\,s^{-1}}$ [39]. Figure 4b shows the products of Hugoniot curves in the P-V plane. As the specific volume becomes smaller, the LX-14 pressure exceeds the PBX 9501 pressure. The value for the pressure at the CJ state given by Dobratz is $P_{\mathrm{CJ}}^{\mathrm{Dobratz}} = 37.0$ GPa and the calibrated value is $P_{\mathrm{CJ}} = 34.9$ GPa.

The Hugoniot U_S-U_P curves for the LX-14 products EOS and reactants EOS are overlayed in Figure 5. The fundamental observation of this plot is that the two equations of state do not cross. This implies that the thermodynamic state of the material, in this case LX-14, is uniquely identified in the U_S-U_P plane in the calibrated EOS models. This may aid the robustness of the calibrated AWSD model in diverse hydrocode simulations.

A complete list of calibrated parameter values for the LX-14 Davis products EOS is given in Table 2.

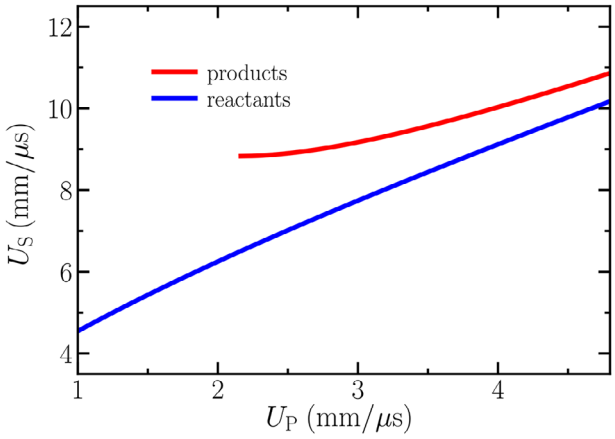

FIGURE 5 | Comparison between U_S-U_P curves for the LX-14 products EOS (red) and reactants EOS (blue).

TABLE 2 | Products EOS parameters.

Parameter	Value	Unit
a	0.8538	
b	0.7142	
k	1.265	
n	1.419	
p_c	6.070	GPa
v_c	0.7182	$\mathrm{cm^{-3}\,g^{-1}}$
C_{vp}	0.001187	$\mathrm{kJ\,g^{-1}\,K^{-1}}$

TABLE 3 | Gas gun data sources for LX-14 from [4]

shot #	$\rho_0(\mathrm{g\,cm^{-3}})$	Impactor	P(GPa)
1S-1612	1.828	Sapphire	2.97
1S-1613	1.828	Sapphire	3.77
1S-1614	1.825	Sapphire	4.78
2S-946	1.828	Kel-F81	6.25
2S-947	1.829	Kel-F81	8.13

2.3 | Rate Law

In the AWSD model, the rate law that describes the rate of change of the mass fraction of product λ at shock temperature T_{shock} and pressure p is

$$\frac{D\lambda}{Dt} = R(T_{\mathrm{shock}}, p, \lambda), \tag{19}$$

where $\frac{D\lambda}{Dt}$ is the material derivative of the product mass fraction and R is the rate. The variable λ is a reaction progress variable that takes a value $\lambda = 0$ when the system consists completely of reactant and $\lambda = 1$ when all the reactant has formed a product. The rate in the AWSD model is given by

$$R = F_p(F_1 + F_2)F_\lambda \tag{20}$$

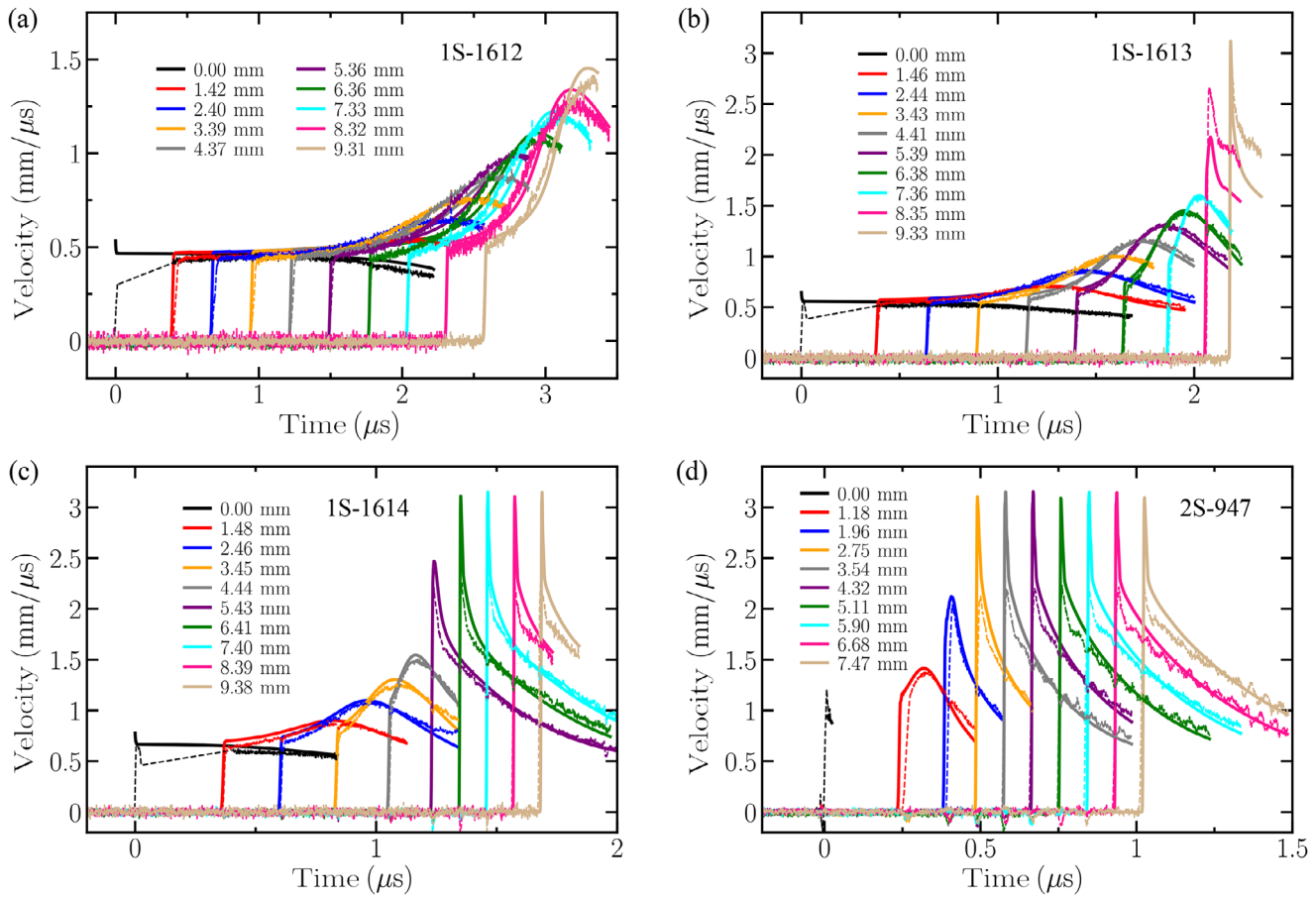

FIGURE 6 | Shock-to-detonation results for the LX-14 AWSD model developed here (solid lines) and experimental data from [4] from embedded electromagnetic gauge experiments (dashed lines) for shots (a) 1S-1612, (b) 1S-1613, (c) 1S-1614, and (d) 2S-947. The locations of the embedded gauges for each shot are shown in the corresponding legend.

TABLE 4 | AWSD parameters for LX-14.

Parameter	Value	Unit
p_s	6.0429	GPa
p_ζ	0.600	GPa
T_1	1267	K
T_2	6187	K
a_1	0.0269	
b_1	2.450	
b_2	0.7335	
δ_λ	0.013	
f_s	0.0115	
k_1	382	μs^{-1}
k_2	2532	μs^{-1}
λ_c	0.980	
n_p	0.942	

where

$$F_p = \begin{cases} \exp[-(p_s/p)^{n_p}], & p > p_\zeta, \\ 0, & \text{otherwise}, \end{cases} \tag{21}$$

$$F_1 = k_1 \exp[-T_1/T_{\text{shock}}](\lambda + a_1 F_p)(1-\lambda)^{b_1}, \tag{22}$$

$$F_2 = k_2 \exp[-T_2/T_{\text{shock}}](1-\lambda)^{b_2}, \tag{23}$$

and

$$F_\lambda = f_s + \frac{1}{2}(1-f_s)\left(1 - \tanh\left[\frac{\lambda - \lambda_c}{\delta_\lambda}\right]\right). \tag{24}$$

Detailed descriptions of what each of these equations physically represent are given in [9]. The AWSD rate law given above has 13 parameters: p_s, p_ζ, T_1, T_2, a_1, b_1, b_2, δ_λ, f_s, k_1, k_2, λ_c, and n_p. The values of these parameters can be assigned by performing a calibration to available data for the specific material being modeled. The data used to perform this calibration typically come from a combination of gas gun and rate stick experimental data.

Jones et al. performed embedded particle velocity gauge measurements of LX-14 at different pressures using gas-gun plate-impact techniques. Five different experiments were performed. A list of those gas gun shots and the pressure of each shot is given in Table 3. We calibrated the rate law parameters in the AWSD model by fitting Equation (19), and the corresponding auxiliary

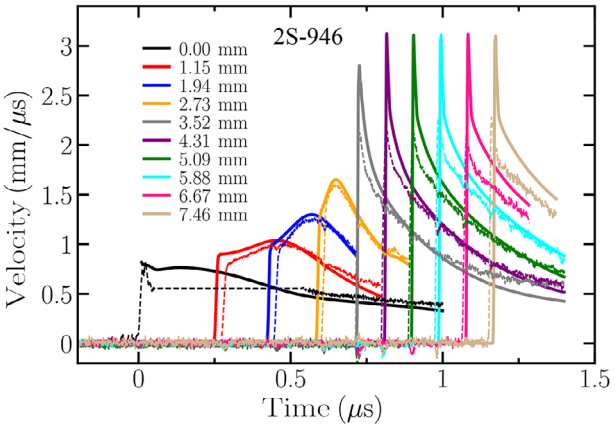

FIGURE 7 | Shock-to-detonation results for the LX-14 AWSD model (solid lines) and experimental data (dashed lines) for shot 2S-946 [4]. This shot was not used in the calibration performed in this work. The locations of the embedded gauges for each shot are shown in the legend.

equations given above, to four of those shots (1S-1612, 1S-1613, 1S-1614, 2S-947). The data from shot 2S-946 was not used in the calibration so that it could be used to validate the developed model.

The rate law parameter calibration was performed in three steps. First, a Nelder–Mead simplex optimization algorithm was used to obtain an initial set of optimized parameter values. This procedure used the experimental gas gun data from shots 1S-1612, 1S-1613, 1S-1614, and 2S-947 as target data. The initial guess for the parameter values used in the optimization was taken to be the PBX 9501 values from [31]. The optimization procedure was performed for 400 iterations. The L^1 error for each gauge and each shot was calculated by comparing the experimental and simulation data. The error values for each gauge and each shot were then combined into a single total error metric. The simplex optimization procedure was employed to obtain the parameter values that minimize this total error. Second, rate-stick experiments were simulated using a shock-fitting code [40]. There is no available rate stick data for LX-14, so we used scaled values for PBX 9404 in the calibration to fill this gap in data. The parameters k_2 and b_2 were calibrated in this second step, while all other parameters were held constant. Third, the same Nelder–Mead simplex optimization procedure described in the first step was performed again, fitting only to gas gun data, to obtain the final parameter values calibrated to experimental results (see Table 4).

Figure 6 shows a comparison between the SDT results predicted by the calibrated LX-14 AWSD model and experimental data from the four shots used in the calibration. The AWSD model is in strong agreement with the experimental results for each shot.

Shown in Figure 6a are the results for shot 1S-1612 which had an initial pressure of 2.97 GPa. The results of low-pressure shots are often difficult to capture using reactive flow simulations, in particular using the AWSD model. This can be observed, for example, in the SURF model results for LX-14. Here, however, the wavefront shapes, initial shock front particle velocities, shock arrival times, and maximum velocity magnitudes predicted by the AWSD model are in excellent agreement with the data for

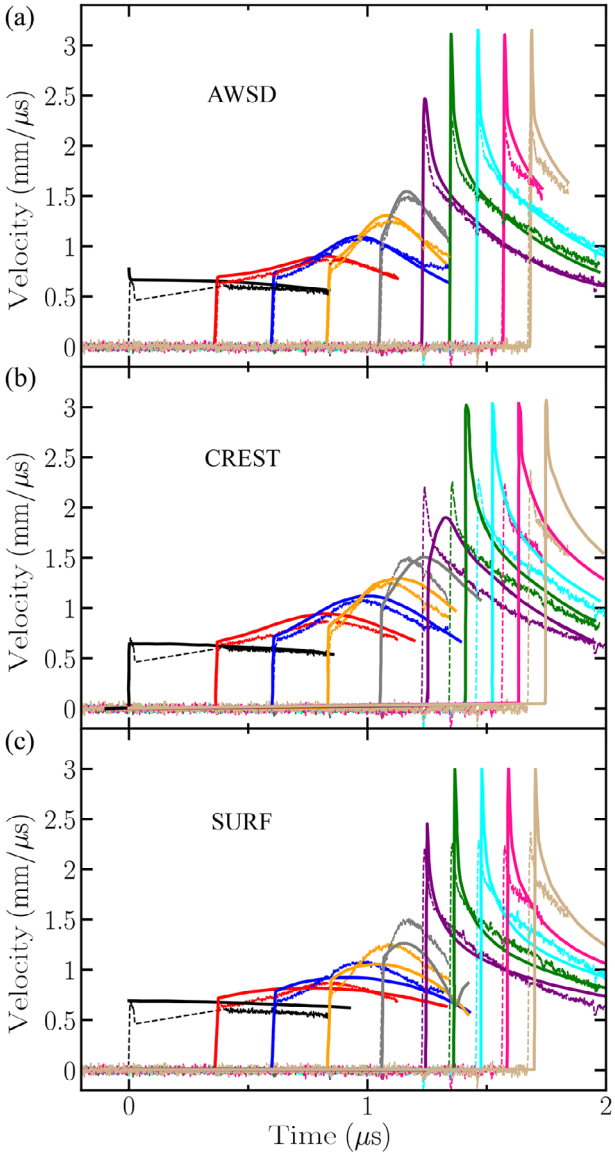

FIGURE 8 | Shock-to-detonation results for shot 1S-1614 using (a) the AWSD model, (b) the CREST model, and (c) the SURF model. In each panel, the solid lines are the results of the respective model and the dashed lines are experimental data from [4].

each gauge. Compared to the CREST model for LX-14, the AWSD model better captures the wavefront shapes for this shot. The AWSD model predicts shock arrival times for each gauge that are in excellent agreement with experiments. The Tarver I&G model estimates slightly later shock arrival times for this shot.

The SDT results for shots 1S-1613 and 1S-1614 are shown in Figure 6b and 6c, respectively. The AWSD model fit to these two shots is excellent, capturing many of the salient shock-to-detonation features including the wavefront shapes, the run-to-detonation times, the shock arrival times for each gauge, and the shock front particle velocities for each gauge. Comparing the CREST results for 1S-1614 and the AWSD result for the same shot, we see that, overall, the AWSD model more accurately captures the experimentally observed behavior. Comparing the AWSD and SURF results for 1S-1613 and 1S-1614, the AWSD result better matches the wavefront shapes. The I&G model

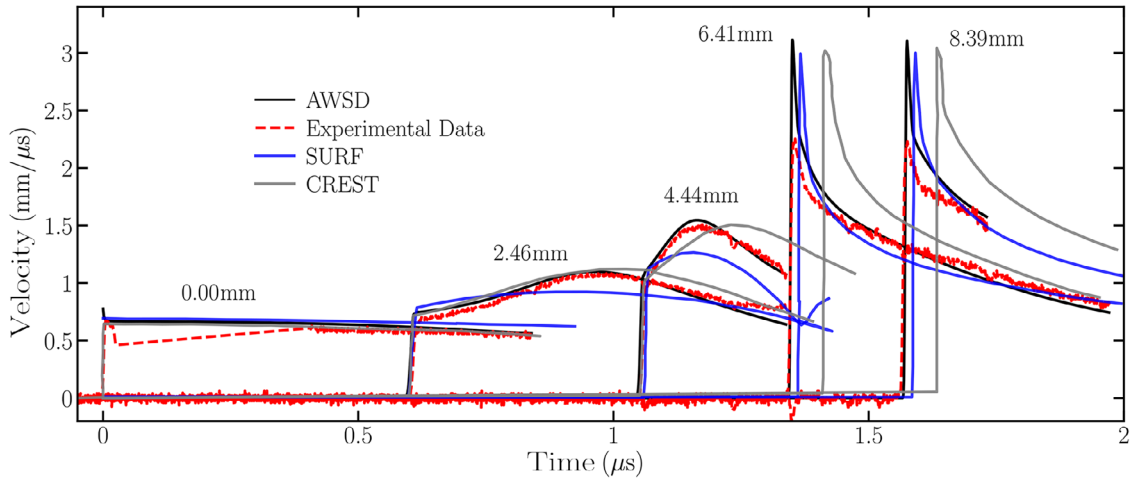

FIGURE 9 | Overlay comparison of shock-to-detonation results for shot 1S-1614 using the AWSD model (black), the CREST model (cyan), and the SURF model (blue). The red dashed lines are experimental data. For visual clarity, only data from every other gauge are shown.

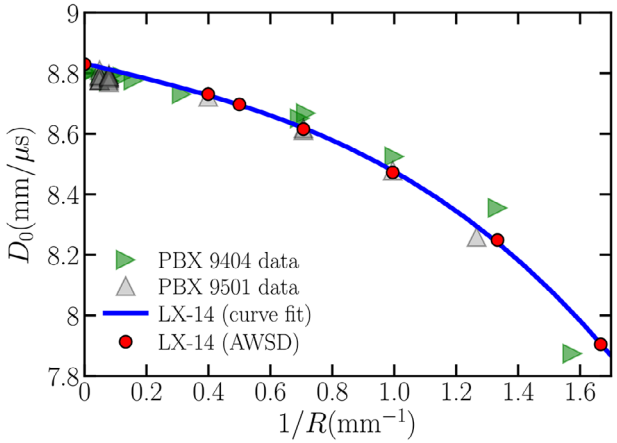

FIGURE 10 | Diameter effect results for LX-14. The gray triangular markers are data for PBX 9501, and the green triangular markers are data for PBX 9404 [41, 42]. The red circular markers are the results of the AWSD simulation with the addition of a point with the detonation velocity for LX-14 of 8.83 mm μs^{-1} from [39]. The blue solid curve is a fit to the simulation results.

by Tarver performs well in predicting the wavefront shapes; however, the shock arrival times predicted by the AWSD model are in better agreement. The shock front particle velocities are generally slightly underestimated by the I&G model while AWSD provides small overestimates. The latter observation appears to be a general phenomenon in AWSD calibrations as it is seen in AWSD models for other HEs [10, 17, 31].

The results for the two-stage shot 2S-947 are shown in Figure 6d. The pressure of this shot was 8.13 GPa. In this high-pressure regime, we again see that the AWSD model captures the behavior of the detonation of LX-14 including the wavefront shapes and the shock arrival times for each gauge.

The experimental wavefront data from shot 2S-946 was not used in the rate law calibration procedure. The results of that shot can therefore be used to validate the calibrated model. The SDT results for shot 2S-946 are shown in Figure 7 and are overlayed with the corresponding experimental results. The predictions generated using the LX-14 AWSD model are in good agreement with the experimental data. This illustrates the predictive capability of the calibrated model on data that were not used to derive values for the model parameters. The shapes of the wavefronts for each gauge are well-captured by the model and are in better agreement with the experimental results than other previous reactive burn models.

A comparison between the AWSD, CREST, and SURF models is given in Figure 8 for shot 1S-1614. We determined that this shot was a good representative example of the difference between the three models. The data for the CREST and SURF models were digitally extracted from the corresponding papers [4, 8]. We do not include a comparison to the Tarver I&G model primarily because the fidelity of the SDT plots in that work makes it difficult to accurately extract the data. Comparing the AWSD model in Figure 8a and the CREST model in Figure 8b, it can be observed that the AWSD model provides a better overall fit to the experimental data. For several of the early gauges in the shot, the CREST model has a good form but it does not transition to detonation as quickly as the experimental data and the detonation lags at a later time. Comparing the AWSD model and the SURF model results in Figure 8c, it can be seen that the SURF model waveform shapes differ slightly from the data as the material transitions to a detonation. Both models agree well with the fully detonating sample.

Figure 9 shows the results of the three models for shot 1S-1614 overlayed along with the corresponding experimental data. Only the data from every other gauge are shown for visual clarity. The AWSD results are shown in black, the CREST results in gray, and the SURF results in blue. The red dashed lines are the experimental data. The results in this figure illustrate the same effects and differences between the models discussed previously. We include this so that the differences between the models are simple to visually ascertain.

The AWSD diameter effect results for LX-14 are shown in Figure 10. The red circular markers are the results of the AWSD simulation and the blue curve is a fit to that simulation data

shown to guide the eye. Experimental data for PBX 9501 and PBX 9404 measured using rate stick experiments are also shown for comparison. The AWSD model predicts that the LX-14 diameter effect behavior will generally fall between the PBX 9501 and PBX 9404 results, the same qualitative behavior predicted by the CREST model.

3 | Conclusions

We have presented the results of an AWSD reactive flow calibration for the HE LX-14. Strong agreement was observed between the calibrated reactive flow model and experimental data for LX-14 from multiple sources [4, 36]. Specifically, the calibrated reactants and products equations of state capture the behavior of thermodynamic data for LX-14 from experimental sources and thermochemical calculations. The shock-to-detonation results generated by the calibrated AWSD model quantitatively capture the time-to-detonation and wavefront shapes of experimental gas gun data. Scaled rate stick data from PBX-based explosives that are chemically similar to LX-14 was used to generate the diameter effect and to calibrate parameters in the AWSD model that depend on these data. In comparison to other reactive flow models for LX-14, the calibrated AWSD model, in general, more accurately captures the shock-to-detonation behavior. Future steps will involve quantifying the uncertainty in the model and the model parameters [43, 44].

Acknowledgments

This work was supported by the U.S. Department of Energy through Los Alamos National Laboratory. Los Alamos National Laboratory is operated by Triad National Security, LLC, for the National Nuclear Security Administration of the U.S. Department of Energy (Contract No. 89233218NCA000001).

Data Availability Statement

The data that support the findings of this study are available from the authors upon reasonable request and institutional approval.

References

1. J. Humphrey, "LX-14: A New High-Energy Plastic-Bonded Explosive," Tech. Rep. UCRL-52350 (Lawrence Livermore National Lab., 1977).

2. F. R. Svingala, R. L. Gustavsen, J. Jones, and A. Houlton, "Plate-Impact Experiments on the HMX-Based Explosive PBX 9404," *AIP Conference Proceedings* 2272 (2020): 030030.

3. M. L. Hobbs, M. J. Kaneshige, W. W. Erikson, and K. T. Meirs, "Gas Retention in an HMX-Based Explosive (LX-14)," *Science and Technology of Energetic Materials* 79 (2018): 35–42.

4. J. D. Jones, X. Ma, B. E. Clements, L. L. Gibson, and R. L. Gustavsen, "Measurement and Reactive Burn Modeling of the Shock to Detonation Transition for the HMX Based Explosive LX-14," *AIP Conference Proceedings* 1979 (2018): 100022.

5. M. J. Burns, "Burns Shock Initiation of Low Density Polymer Bonded Explosive LX-14: A Study of Two Morphologies," *Journal of Applied Physics* 131 (2022): 145103.

6. K. S. Vandersall, M. R. DeHaven, S. L. Strickland, C. M. Tarver, H. K. Springer, and M. R. Cowan, "Shock Initiation Experiments With Ignition and Growth Modeling on the HMX-Based Explosive LX-14," *AIP Conference Proceedings* 1979 (2018): 100045.

7. C. M. Tarver, "Ignition and Growth Modeling of Shock Initiation Using Embedded Particle Velocity Gauges in the Plastic Bonded Explosive LX-14," *Journal of Energetic Materials* 39 (2021): 494–505.

8. C. Handley and N. Whitworth, "A CREST Reactive Burn Model for LX-14," *AIP Conference Proceedings* 2844 (2023): 290003.

9. T. D. Aslam, "Shock Temperature Dependent Rate Law for Plastic Bonded Explosives," *Journal of Applied Physics* 123 (2018): 145901.

10. M. A. Price, J. A. Leiding, T. D. Aslam, et al., "A Reactive Flow Model for the 3,3'-Diamino-4,4'-Azoxyfurazan Based Plastic Bonded Explosive (PBX 9701)," *Journal of Applied Physics* 130 (2021): 215903.

11. R. Menikoff, "Arrhenius Rate: Constant Volume Burn," Tech. Rep. LA-UR-17-31024 (Los Alamos National Laboratory, 2017).

12. R. C. Huber, J. Peterson, J. D. Coe, et al., "Polysulfone Shock Compressed Above the Decomposition Threshold: Velocimetry and Modeling of Two-Wave Structures," *Journal of Applied Physics* 127 (2020): 105902.

13. G. T. Craven, "Analytical Solutions of the Arrhenius-Semenov Problem for Constant Volume Burn," Tech. Rep. LA-UR-21-31229 (Los Alamos National Laboratory, 2021).

14. W. C. Davis, "Equation Of State for Detonation Products," *Paper Presented at the 8th Symposium on Detonation*, Albuquerque, NM, July 15–19, 1985.

15. W. C. Davis, "Equation of State for Detonation Products," *Paper Presented at the 10th Detonation Symposium*, Boston, MA, July 12–16, 1993.

16. W. C. Davis, "Equation of State for Detonation Products," *Paper Presented at the 11th International Detonation Symposium*, Snowmass Village, CO, Aug. 31–Sept. 4, 1998.

17. C. Ticknor, S. A. Andrews, A. Henrick, et al., "A Burn Model for Trinitrotoluene (TNT)," *AIP Conference Proceedings* 2844 (2023): 300020.

18. M. Z. Bazant, "Theory of Chemical Kinetics and Charge Transfer Based on Nonequilibrium Thermodynamics," *Accounts of Chemical Research* 46 (2013): 1144–1160.

19. G. T. Craven and R. Hernandez, "Lagrangian Descriptors of Thermalized Transition States on Time-Varying Energy Surfaces," *Physical Review Letters* 115 (2015): 148301.

20. G. T. Craven and A. Nitzan, "Electron Transfer Across a Thermal Gradient," *Proceedings of the National Academy of Sciences* 113 (2016): 9421–9429.

21. D. V. Matyushov, "Activated Kinetics in a Nonequilibrium Thermal Bath," *Proceedings of the National Academy of Sciences* 113 (2016): 9401–9403.

22. I. Santamaría-Holek and A. Pérez-Madrid, "Eyring Equation and Fluctuation-Dissipation Far Away From Equilibrium," *Journal of Chemical Physics* 153 (2020): 244116.

23. C. M. Tarver, J. W. Forbes, and P. A. Urtiew, "Nonequilibrium Zeldovich-von Neumann-Doring Theory and Reactive Flow Modeling of Detonation," *Russian Journal of Physical Chemistry B* 1 (2007): 39–45.

24. R. Menikoff, "On Beyond the Standard Model for High Explosives: Challenges & Obstacles to Surmount," *AIP Conference Proceedings* 1195 (2009): 18–25.

25. O. Kunova, E. Nagnibeda, and I. Sharafutdinov, "Non-Equilibrium Reaction Rates in Air Flows Behind Shock Waves. State-to-State and Three-Temperature Description," *AIP Conference Proceedings* 1786 (2016): 150005.

26. R. Menikoff, "Detonation Wave Profile," Tech. Rep. LA-UR-15-29498 (Los Alamos National Laboratory, 2015).

27. R. Menikoff, "Introduction to High Explosives." Tech. Rep. LA-UR-19-20814 (Los Alamos National Laboratory, 2019).

28. J. H. Peterson and J. D. Coe, "Beyond the Arrhenius Rate law in Simulating the Shock-Driven Decomposition of Polyimide," Tech. Rep. LA-UR-20-20313 (Los Alamos National Laboratory, 2020).

29. C. Ticknor, S. A. Andrews, and J. A. Leiding, "Magpie: A New Thermochemical Code," *AIP Conference Proceedings* 2272 (2020): 030033.

30. T. D. Aslam, "A Recipe for Implementing the Arrhenius-Shock-Temperature State Sensitive WSD (AWSD) Model, With Parameters for PBX 9502," Tech. Rep. LA-UR-17-24003 (Los Alamos National Laboratory, 2017).

31. T. D. Aslam, M. A. Price, C. Ticknor, J. D. Coe, J. A. Leiding, and M. A. Zocher, "AWSD Calibration for the HMX Based Explosive PBX 9501," *AIP Conference Proceedings* 2272 (2020): 030001.

32. R. Menikoff, "Detonation Waves in PBX 9501," *Combustion Theory and Modelling* 10 (2006): 1003–1021.

33. M. J. Cawkwell, M. Zecevic, D. J. Luscher, and K. J. Ramos, "Complete Equations of State for Cyclotetramethylene Tetranitramine," *Propellants, Explosives, Pyrotechnics* 46 (2021): 705–712.

34. S. P. Marsh, *Lasl Shock Hugoniot Data*. (University of California Press, 1980).

35. J. J. Dick, A. R. Martinez, and R. S. Hixson, "Plane Impact Response of PBX 9501 and Its Components Below 2 GPa," Tech. Rep. (Los Alamos National Laboratory, 1998).

36. L. Green, N. Holmes, and J. Kury, "Shock Measurements on Explosives in the Supra Compressive Region," *International Symposium on Pyrotechnics and Explosives* 1195 (1987): 129–132.

37. J. N. Fritz, R. S. Hixson, M. S. Shaw, C. E. Morris, and R. G. McQueen, "Overdriven-Detonation and Sound-Speed Measurements in PBX-9501 and the "Thermodynamic" Chapman–Jouguet Pressure," *Journal of Applied Physics* 80 (1996): 6129–6141.

38. E. R. Pittman, C. R. Hagelberg, R. L. Gustavsen, and T. D. Aslam, "Gas Gun Experiments and Numerical Simulations on the HMX Based Explosive PBX 9501 in the Overdriven Regime," *AIP Conference Proceedings* 1979 (2018): 150032.

39. B. M. Dobratz, *LLNL Explosives Handbook: Properties of Chemical Explosives and Explosives and Explosive Simulants* (Lawrence Livermore National Lab., 1981).

40. C. M. Romick and T. D. Aslam, "High-Order Shock-Fitted Detonation Propagation in High Explosives," *Journal of Computational Physics* 332 (2017): 210–235.

41. L. Hill, "Compilation of Ambient PBX-9501 Detonation Speed Data," Tech. Rep. (Los Alamos National Laboratory, 2012).

42. T. Gibbs and A. Popolato, *LASL Explosive Property Data* (University of California Press, 1980).

43. S. A. Andrews and A. M. Fraser, "Estimating Physics Models and Quantifying Their Uncertainty Using Optimization With a Bayesian Objective Functional," *ASME Journal of Verification Validation and Uncertainty Quantification* 4 (2019): 011002.

44. S. A. Andrews, J. A. Leiding, J. Thrussell, and C. Ticknor, "Calibration and Uncertainty Quantification for Davis Equation of State Models for the High Explosive PBX 9501 Products," *Propellants, Explosives, Pyrotechnics* 49 (2024): e202300110.